JOURNAL OF RESEARCH of the National Bureau of Standards—A. Physics and Chemistry
Vol. 69A, No. 3, May–June 1965

Observations of Dislocations and Surface Features in Corundum[1] Crystals by Electron Transmission Microscopy

D. J. Barber and Nancy J. Tighe

(February 12, 1965)

Crystals of corundum, grown by the flame-fusion method, have been chemically thinned and examined by electron transmission microscopy. Some specimens were etch-pitted after thinning, and the relationship between etch pits and dislocations was investigated. Within subgrains there is a close agreement between dislocation and etch pit densities; this agreement breaks down along many boundaries. The etching behavior of crystals containing Cr_2O_3, TiO_2 and other impurities has been examined. Etch-tunneling along grown-in dislocations is commonly observed in the impurity-doped materials; it is particularly pronounced in ruby. In heat-treated crystals containing TiO_2, local differences in solid solubility can lead to the formation of etch hillocks. Thermally etched surfaces have also been characterized, and gas atmospheres are shown to affect the surface topology. Evaporation experiments in the electron microscope are reported.

1. Introduction

In recent years, etch-pitting techniques have been used extensively [1, 2][2] to investigate dislocation behavior in inorganic crystals. These methods have been supplemented and made more meaningful by the advent of x-ray topographic and electron microscope studies. The discovery of solid state laser action in certain impurity-doped crystals, and the dependence of laser efficiency on dislocation density and freedom from gross defects, has stimulated interest in etching techniques. Crystals intended for laser applications include molybdates, tungstates, and aluminum oxide containing chromium oxide (ruby).

Currently much effort is directed towards growing crystals with low dislocation densities and the densities are commonly estimated by etch-pitting methods. This paper describes how etch pits and other surface features are related to internal defects in both pure and doped corundum crystals. An examination of dislocation behavior in corundum, using electron transmission microscopy, is published elsewhere [3]. It is hoped that our results will add significantly to the data previously obtained from deformation, x-ray and surface studies.

Wachtman and Maxwell [4], Klassen-Neklyudova [5], and Scheuplein and Gibbs [6] have studied the deformation behavior of single crystal sapphire. It is recognized that two mechanisms exist for plastic deformation by dislocation glide. Near to its melting point, sapphire can slip on the $\{1\bar{2}10\}$ prism planes, in the $\langle 10\bar{1}0 \rangle$ directions; this will be referred to as prism plane glide. More commonly, slip occurs on the $\{0001\}$ planes in the $\langle 11\bar{2}0 \rangle$ directions; this is known as basal glide and can occur at temperatures as low as 900 °C.

Chemical etching of sapphire was first investigated by Seebach [7], who used a potassium bisulfate flux to obtain etch-pitted surfaces and terminal dissolution bodies. More recently, Scheuplein and Gibbs [6], and Stephens and Alford [8] have used phosphoric acid and bisulfate fluxes for etching studies. Palmour [9] has studied the appearance of thermally etched surfaces.

2. Experimental Procedure

Specimens of white sapphire and ruby were cut from 1/8-in. or 1/10-in. rods, grown by the Verneuil method, and supplied by the Adolf Meller Company. Impurity-doped boules grown at the National Bureau of Standards were also investigated.

The technique used for thinning sections of bulk sapphire has been described by Tighe [10]. Chemical polishing is carried out with hot phosphoric acid, initially by total immersion, and finally with a chemical jet device which affords precise control over the thinning process. By feeding fresh acid into the device, the jet is sustained until a hole appears in the sample; normally the hole is bounded by areas sufficiently thin to transmit electrons. Experiment showed that different temperatures were needed to polish the various low index crystallographic planes. Sections cut parallel to basal or rhombohedral $\{10\bar{1}2\}$ planes polish at 450 to 460 °C; parallel to prism $\{10\bar{1}0\}$, $\{11\bar{2}0\}$ planes and scalenohedral $\{12\bar{3}4\}$ planes, polishing occurs at 500 to 510 °C. Pronounced etching occurred at temperatures ~50 °C below the optimum polishing tempera-

---

[1] Corundum is pure aluminum oxide, Al_2O_3, in the stable α-phase. The term sapphire is used synonymously in this paper. Crystallographic indices are referred to the structural unit cell, $c/a = 2.730$.

[2] Figures in brackets indicate the literature references at the end of this paper.

ture for each orientation. Light etch-pitting could be achieved, therefore, by lowering the acid temperature as the thinning process neared completion.

The operation of the jet-polishing device depends on the condensation and boiling of orthophosphoric acid. Fresh acid is supplied to sustain operation but, since some acid also recirculates, reaction products build up in solution. If polishing is maintained too long, phosphate deposits can occur on the specimens. Although this can be avoided with care, prolonged boiling in aqua regia is sometimes necessary to obtain absolutely clean surfaces.

Certain specimens, discussed in the text, were chemically etched after normal chemical thinning, using very concentrated hot potassium hydroxide. For other work, described in section 3.4, thinned samples were further thinned by surface evaporation under various gas atmospheres. Specimens were either supported on a resistively heated carbon tape or placed in an alumina boat in a platinum-wound resistance furnace.

Charging of the samples in the electron microscope was avoided by evaporating ~ 100 Å of carbon on to the flat side of each specimen, and placing this side on a copper grid. The microscope, a JEM 6A, was operated at 100 kV.

3. Results

3.1. Characteristics of Chemical Etch Pits

The general features of etch-pitted sapphire surfaces have been described by Scheuplien and Gibbs [6], and by Alford and Stephens [8]. These workers have measured the dislocation densities for typical material grown by flame-fusion, and found these to be in the range 10^5–10^6/cm^2. Many of the dislocations are in subgrain boundary arrays which are approximately perpendicular to the {0001} planes. With phosphoric acid, the etching times must be short in order to retain pits which are small enough for satisfactory electron microscopy. Even then, the pits are somewhat ill-defined, as indicated by figure 1; this shows etch pits on an array of dislocations. The diffraction contrast indicates that the dislocations are nearly perpendicular to the specimen plane, which is {0001}. The array is therefore composed of prism plane dislocations of edge character and is nearly a pure tilt boundary. To estimate the order of the misorientation, a Burgers vector $b_{[10\bar{1}0]} = 8.22$ Å is assumed; the dislocation spacing of 1μ then implies a misorientation of ~ 3 min of arc. Etch pits produced on pure sapphire by phosphoric acid are somewhat less well defined than their counterparts on ruby (Al_2O_3 containing a small amount of Cr_2O_3). Figure 2 shows two etch pits on the same face of an {0001} specimen of ruby ($Al_2O_3 + 2$ wt percent Cr_2O_3 in feed powder for flame fusion), with a short segment of dislocation looping between them. It has been found that the pyramidal pits are rotated by 180° with respect to one another on the opposing faces of a {0001} section. This rotation reflects the essentially trigonal nature of the crystal. The etch pit edges are approximately parallel to $\langle 11\bar{2}0 \rangle$ directions. It is significant that the small segment of dislocation is retained in the specimen, between the etch pits. Its presence lends support to other evidence [3] that plastic deformation in sapphire does not occur at normal temperatures. In materials where room temperature deformation occurs, small half-loops may 'pop' out of the surface.

It was sometimes found that etch pits in white sapphire exhibited short 'tails' leading from their apices into the crystal interior. These small tails, on enlargement, are the 'beaks' described by Honess [11], which are a feature of etch pits on many natural mineral crystals. These 'beaks' are now commonly recognized as occurring in etched crystals containing trace impurities. They are undoubtedly due to attack along dislocations decorated with impurity particles, or dislocations with impurity atmospheres. In impurity-doped corundum, the occurrence of etch pits with tails is more pronounced; the tails appear as small tunnels into the crystal. The effect is found in samples containing ThO_2, La_2O_3, and Cr_2O_3; it is particularly pronounced in ruby. The effect is discussed at length in section 3.3. For convenience in illustration, a basal section of pink ruby was chosen to show the appearance of short etch tunnels, or tails, in figure 3. The occurrence of etch pits originating on both the upper and lower crystal surfaces should also be noted.

Etch pits produced in hot caustic potash solution differ markedly from the rounded and somewhat poorly defined ones obtained with phosphoric acid. On the basal plane, 'alkali' pits are almost always hexagonal in shape; they are deep and they undergo less lateral spread than the 'acid' etch pits. It is thus common to find pits passing right through the thicker parts of specimens at points where dislocations were almost normal to the surface. Figure 4 shows a bright field transmission micrograph to illustrate this point. It closely parallels the case of rutile, TiO_2, thinned in a sodium hydroxide flux, observed by Barber and Farabaugh [12]. The highest orders of the electron extinction fringes are not visible in the reproduction; on the original photographic plate, however, six contour fringes are visible around the pits. The plate was obtained for two beam diffraction with a $11\bar{2}0$ reflection operating. Values of extinction distance, t_0, have been calculated for several lattice reflections and these are given in the appendix. The electron image thus indicates that the specimen thickness at the etch pits was approximately 7560 Å. This agrees quite well with the value deduced from the pattern of optical interference fringes seen in this specimen, 8400 Å. The measurement was made using blue light of wavelength 4600 Å, assuming a value of 1.760 for the refractive index. Taking account of the possible relativistic correction to the electron accelerating potential, mentioned in the appendix, the values agree to within 100 Å.

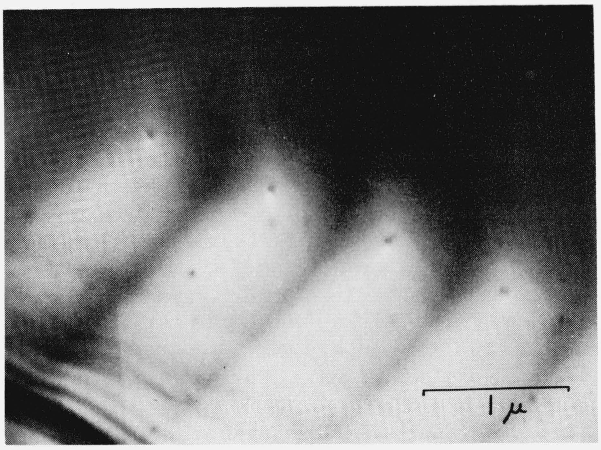

Figure 1. *Prism plane dislocations and associated etch pits in a {0001} section.*

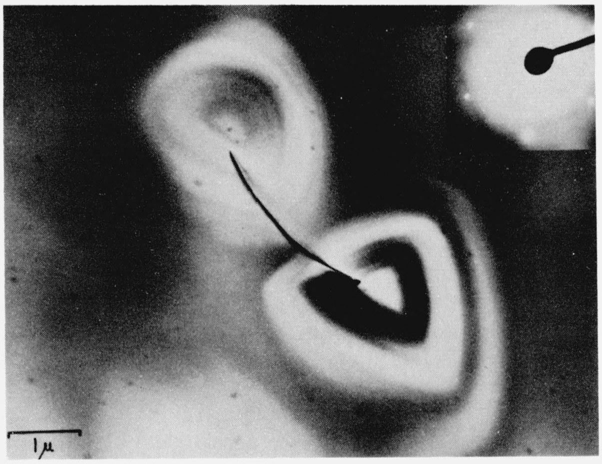

Figure 2. *Segment of dislocation looping between two etch pits on the same {0001} surface of a ruby crystal etched in hot phosphoric acid.*

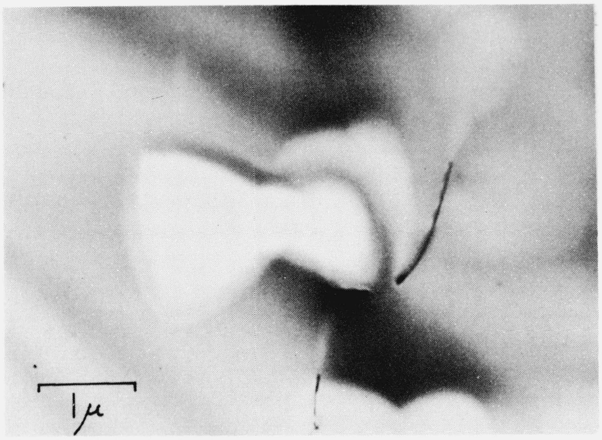

Figure 3. *Surface etch pits and short etch tunnels in a sample of ruby; the black lines are dislocations.*

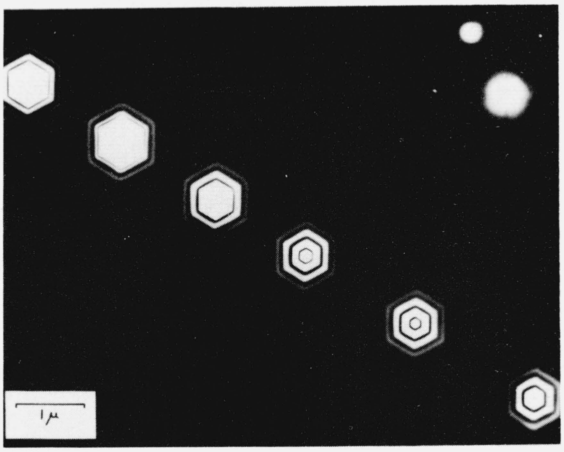

Figure 4. *Hexagonal etch pits on a subgrain boundary in a {0001} section etched in hot potassium hydroxide, $11\bar{2}0$ reflection operating.*

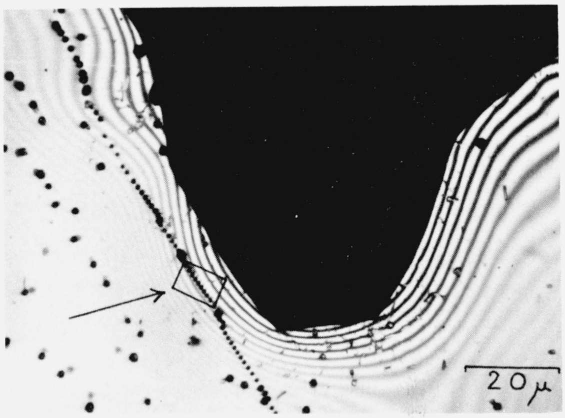

Figure 5. *Reflection optical micrograph of general area shown in figure 4, taken with green light.*

The 'alkali' etch pits shown in figure 4 have their edges strictly parallel to $<10\bar{1}0>$ directions. The fact that phosphoric acid etch pits are three-sided, whilst those produced in potassium hydroxide are six-sided, stems from the existence of only three crystallographically equivalent_ *a*-directions, as compared with six equivalent $<1010>$ directions. Moreover, unlike the pits produced by phosphoric acid, the shape of these pits is strongly affected by the inclination of the dislocations to the surface so that they often exhibit a marked asymmetry. The appearance of the field shown in figure 4, both in the electron microscope and in the optical microscope (figure 5, reflection micrograph, green light) leads to the conclusion that the pits delineate the emergence points of dislocations in a subgrain boundary.

3.2. Correspondence Between Etch-Pit Density and Dislocation Density

During this work, the relationship between surface etch pits and internal dislocation arrangements has been examined. As might be expected, etch pits are often found in very thin areas of the crystal where the dislocations have been etched out. Occasionally other pits are found which do not pass through the section, but which could have been associated with a loop or a small crystal void. On the other hand, it is invariably found that, within grains and subgrains, every dislocation which meets the surface is accompanied by an etch pit. At first sight, therefore, there appears to be a good correspondence between dislocation and etch-pit density. In view of our examination of subgrain boundary etching, however, this conclusion must be modified.

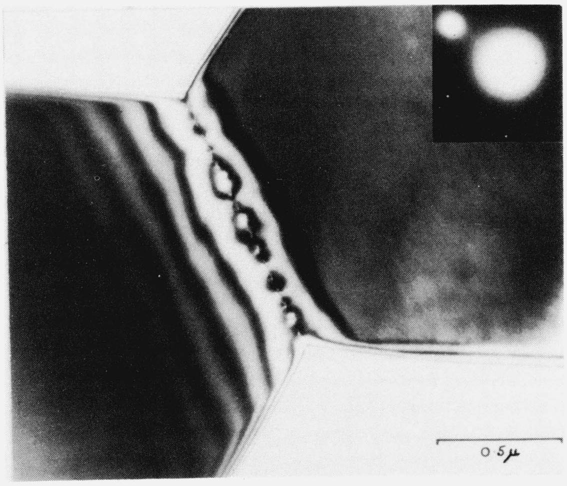

FIGURE 6. *Dislocations perpendicular to the surface in the join between two large hexagonal etch pits in a {0001} section.*

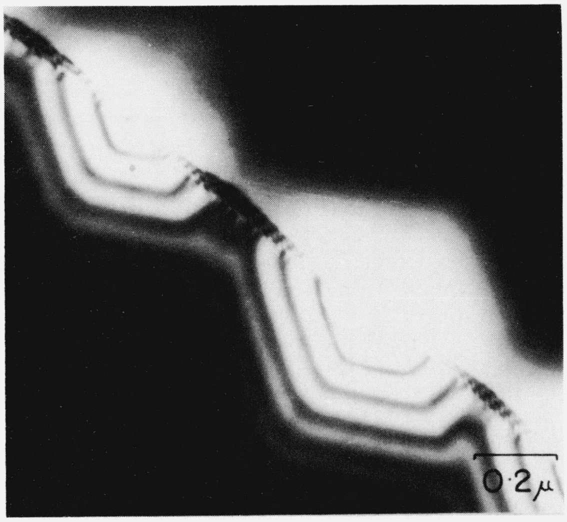

FIGURE 7. *Hexagonal etch pits on a steeply inclined twist boundary in a {0001} section, $30\bar{3}0$ reflection operating.*

For a considerable number of the boundaries investigated it was noted that the etch-pit density along the boundary did not accurately reflect the dislocation spacing. Often the dislocations are grouped within the boundary and there is only one etch pit per dislocation group. The areas between the pits may be slightly grooved but no individual pits are visible in the optical microscope; they are seldom apparent in the electron microscope. The effect is illustrated by figure 6. It shows a number of dislocations, normal to the {0001} specimen surface, in one of the joins between a succession of large etch pits of the type shown in figure 4; the joins had etched to give shallow v-grooves. In figure 6 the slight groove gives rise to several equal thickness fringes. The fringe at the bottom of the groove is discontinuous and follows the array of short dislocation segments. The line of dislocations is parallel to a $< 10\bar{1}0 >$ direction; thus, they must lie in a $\{1\bar{2}10\}$ plane and they are prism plane dislocations. The lack of correspondence between pits and dislocations along boundaries may be specifically associated with boundaries of mixed character or with composite boundaries formed by the climb of arrays of different ages. Figure 7 shows a twist-type boundary (one set of dislocations showing only weak contrast), with etch pits at regular but infrequent intervals. By tilting the specimen, the extinction fringes could be displaced from one side of the boundary to the other. Locally, the crystal was 17,000 Å thick (calculated from optical interference pattern). A possible explanation may be that the boundary formed as the result of the climb of a twist-net until the latter encountered a preexisting array of dislocations; on etching, only the older dislocations in the composite boundary were attacked.

Although the above examples are boundaries which have been etched in potassium hydroxide, the breakdown in dislocation — etch pit correspondence is not restricted to this etchant. We have noted similar behavior using phosphoric acid as the etchant. Because the etch pits formed with phosphoric acid are poorly defined, however, the result is harder to demonstrate with micrographs. Nonetheless, our observations cast doubt on the validity of etch-pit counts along grain boundaries in sapphire crystals, and this must have an effect on the accuracy of total dislocation density estimates.

3.3. Chemical Etching of Impurity-Doped Aluminum Oxide

The etchants used for white sapphire were also effective with ruby, star sapphire ($Al_2O_3 + 0.25$ wt % TiO_2), and other impurity-doped materials. The etching effect is more pronounced and the etch pits more clearly defined. The impurity-doped crystals often contain a number of low angle grain boundaries, and these boundaries usually etch into deep grooves. The etching reveals, moreover, that in some materials (e.g., $Al_2O_3 + 0.25$ wt % GeO_2) the boundaries often contain many small cavities.

The etching characteristics of two impurity materials are of particular interest:

Ruby, $Al_2O_3+Cr_2O_3$. The etching characteristics have been noted briefly in section 3.1. The production of long etch tunnels is particularly striking. They may penetrate as much as 5 μ from the crystal surface and narrow to ~ 500 Å at the etching tip. Figure 8 is clear evidence that the tunnels follow the paths of dislocations. Well within the crystal, a dislocation is seen continuous with the narrow tunnel.

Recently it has been found that etch tunnels occur in other synthetic nonmetallic crystals. In magnesium fluoride, MgF_2, thinned in hot sulfuric acid, Barber [13] has found tunnels as long as ~ 50 μ, with diameters as small as ~ 300 Å. The larger tunnels are now known to result from etching along grown-in dislocations decorated with small magnesium oxide precipitates (which can be seen in the ultramicroscope). The very smallest tunnels are thought to result from etching dislocations with unseen impurity atmospheres. In magnesium fluoride the tunnels have near-constant diameters, whilst in ruby the tunnels are enlarged near the surface. This can be attributed to the different etching rates of the two materials. The tunnels in magnesium fluoride form in a matter of seconds and there is little time for differential lateral spread; in ruby, the tunnels take many minutes to form.

The occurrence of strong etch tunneling in ruby leads us to postulate that, although all compositions of the Al_2O_3–Cr_2O_3 system are believed to be solid solutions [14], this is not realized in practice. Under the growth conditions for flame fusion crystals, it appears that either impurity atmospheres or microsegregates of chromic oxide occur along grown-in dislocations.

Star sapphire, $Al_2O_3+0.25$ wt percent TiO_2. Crystals were grown and then heat-treated for 24 hr at 1300 °C to produce precipitated or 'star' sapphire. The resulting material contained a high density of precipitate needles, commonly thought to be rutile, TiO_2 [15]. Recently Irving [16], using an electron probe analyzer, has found the needles to be an aluminum titanate. The crystals were thinned, under both etching and polishing conditions, and examined. The precipitate needles were not markedly attacked by hot phosphoric acid, and many were retained in even the thinnest regions of the sapphire matrix crystal.

The general appearance of the thinned crystal is shown in the optical micrograph of figure 9. This shows a basal section, the needle axes being parallel to $< 10\bar{1}0 >$ directions. The specimen also exhibited some unexpected features, namely the triangular and bullet-shaped areas visible in the figure. By electron microscopy, the strange appearance of the thinned crystal is easily explained. Parts of a typical precipitated sample, viewed by electron transmission, are shown in figure 10. Figure 10a shows several bullet-shaped lozenges and a number of well defined needles; often needles are seen within the diffuse lozenges. Rounded-off lozenges were often left projecting over the edges of the thinned specimens, as shown in figure 10b, and these were carefully examined. Selected area diffraction, and the appearance of equal thickness fringes, showed that the lozenges and triangles have the corundum structure. Thus they are not actual precipitates, neither are they a direct result of the precipitation process.

Observations on the sharply defined needles suggest that these are the true precipitates. They are usually parallel-sided, but kinked examples are occasionally found. The sharpness of the boundaries defining the precipitate is illustrated in figure 11. This shows the effect of etching a thinned sample in hot concentrated potassium hydroxide (~ 250 °C) for 10 min. Apparently the needle shown emerges on the two crystal surfaces; pits form at both ends and the etchant starts to produce tunnels at *A* and *A′* by attacking the precipitate. Conclusive identification of the needle material by selected area diffraction has not yet been achieved.

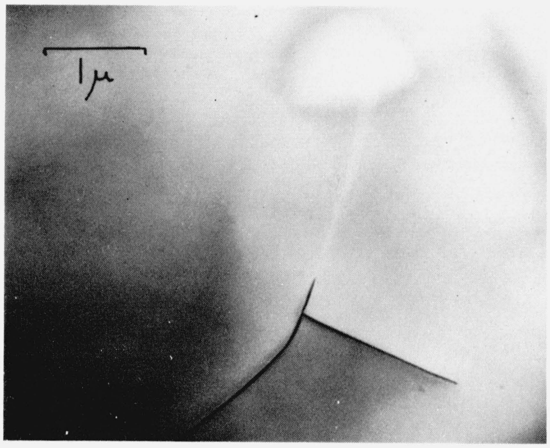

FIGURE 8. *Etch pit and etch-tunnel associated with a dislocation in ruby.*

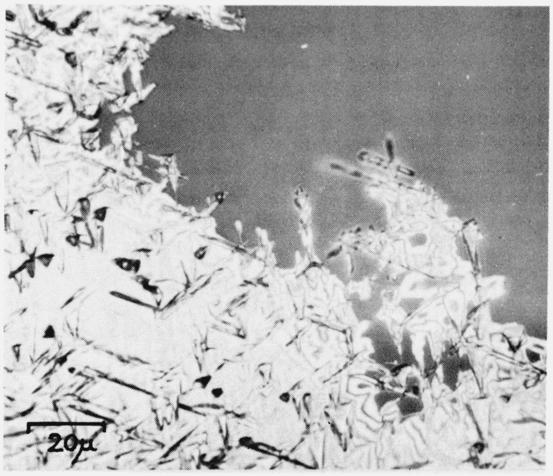

FIGURE 9. *Optical reflection micrograph of thinned heat-treated sample of star sapphire.*

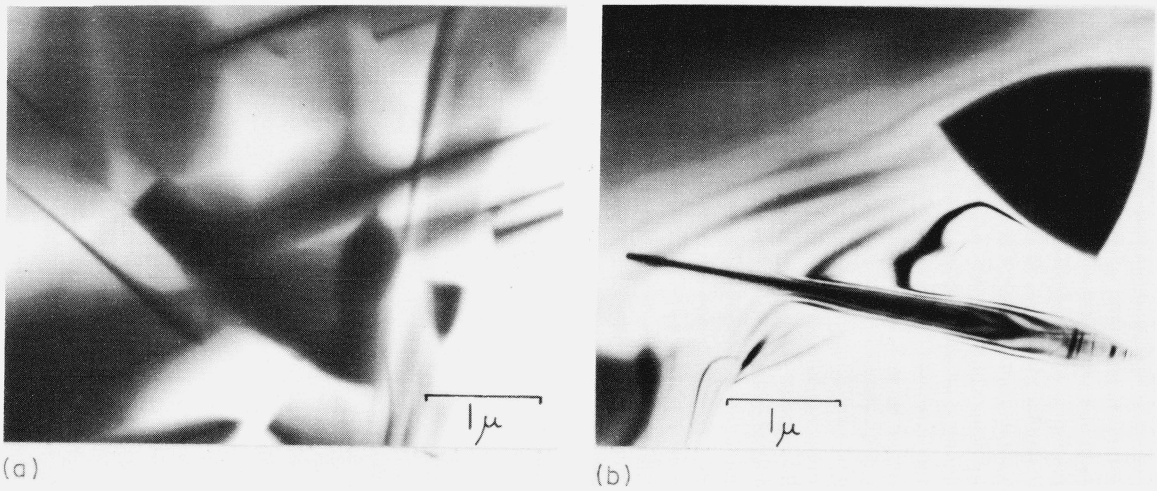

FIGURE 10. *Transmission electron micrographs: (a) showing general appearance of thinned heat-treated sample of star sapphire (b) showing features at edge of thinned crystal.*

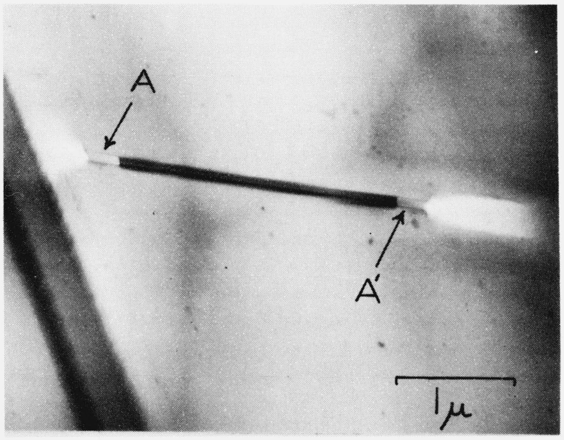

FIGURE 11. *Etch-pits produced at the extremities of a precipitate needle by the action of hot potassium hydroxide.*

The lozenge-shaped and triangular features were judged, from their opacity and from thickness fringes, to be etch hillocks. They result from a local decrease in etching rate around needles. There are three possible explanations for their occurrence: (a) the needles are surrounded by material depleted in solute; (b) the needles are surrounded by material rich in solute; (c) the slowly dissolving needles produce a somewhat insoluble reaction product which adheres to the surrounding surface and thus inhibits attack. Explanation (a) is more plausible than (b) since it is known that impurity-doped material has a higher chemical potential than pure material, and is thus more readily attacked. It is also found, however, that titanium compounds have a tendency to form gummy sols which can markedly affect dissolution characteristics (Barber and Farabaugh [12]); hence explanation (c). These sols are usually in evidence after thinning, however, and there is virtually no evidence for their presence on the star sapphire specimens. It is therefore concluded that the occurrence of the etch hillocks is best explained by the assumption of a solute-depleted zone around the precipitate needles. The occurrence of the bullet-shaped features is easily explained. Any isolated center of solute depletion will decrease the local etching rate and produce a triangular hillock, since this reflects the basic etching habit of the basal plane. After the disturbance is removed, the hillock will slowly shrink and disappear as etching proceeds. If a precipitate needle, and its attendant depleted zone, meets the specimen surface at an acute angle, then the etching center will move with time. Figure 12 shows schematically how the change in the position of a triangular hillock with time will lead to a bullet-shaped hillock.

This adequately explains that elongated hillocks form by the etching action around needles but it does not explain the triangular hillocks themselves. Since there are no needles formed parallel to the <0001> direction, one might suppose that the crystals contain non-needlelike particles of precipitate which produce triangular hillocks. Observations in the optical microscope reveal a number of small triangular precipitates which appear to arise from the contact of two or more embryo needles. Examples are visible

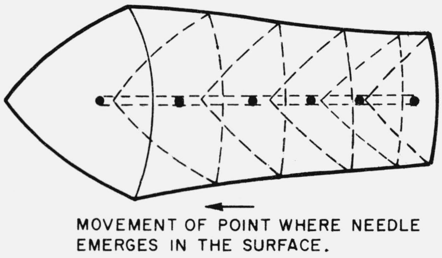

FIGURE 12. *Diagram to show the formation of bullet-shaped hillocks by selective etching around the sites of precipitate needles.*

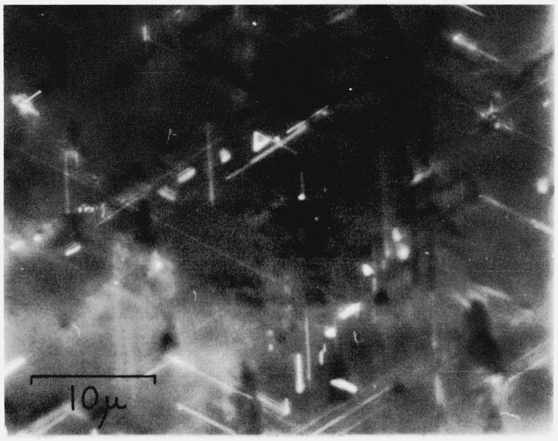

FIGURE 13. *Optical reflection micrograph taken with oil immersion objective to show small triangular precipitates within crystal of star sapphire.*

in figure 13. Further evidence for their occurrence, and incidental confirmation that the hillocks are sapphire, has been obtained by heating and cooling samples in the microscope to dissolve and then reprecipitate needles. These observations, and some relating to dislocations in star sapphire, will be discussed in another publication.

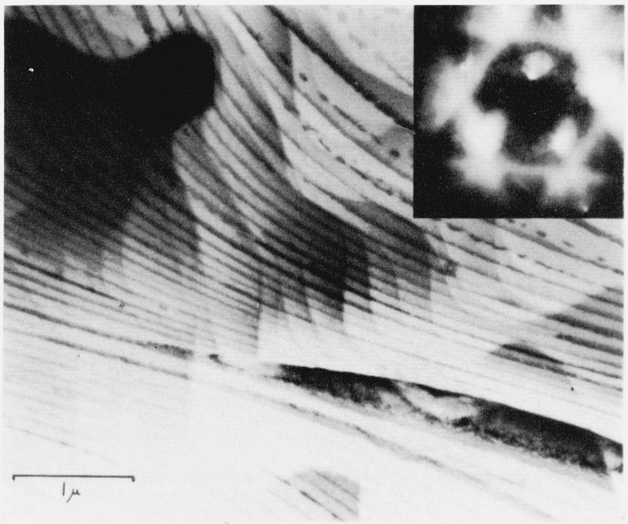

FIGURE 14. *Surface terraces and 'contamination' on a {0001} section thinned by heating in a mixture of argon and nitrogen for 4 min at 1900 °C.*

3.4. Thermal Etching Observations

To examine the dependence of surface characteristics on internal perfection and surface environment, samples which had been partially thinned by chemical means were subjected to different thermal treatments in gas atmospheres. Figure 14 is a transmission micrograph of a {0001} section after heating in a mixture of argon and nitrogen gases at 1900 °C for 4 min and quenching into liquid nitrogen. A large number of curving surface terraces are to be seen, most of these being decorated by small islands of porous-looking material. From diffraction data, it was concluded that this material is principally Al_2O_3, but it may not be the α form. Wachtman and Maxwell [4] found that sapphire rods were covered with a whitish deposit after annealing in argon; from x-ray diffraction data, the deposit was thought to be γ-alumina. In other specimens held at 1980 °C, terrace decoration was largely absent but large globules were present. There was no evidence to connect these surface features with internal defects. Once again, terraces did not follow crystallographic directions. Occasionally, however, hexagonal plateaus and spirals were found on the surfaces, and whiskers were often found to grow from the centers of the hexagons. Other workers have made similar observations on sapphire platelets grown by the oxidation of aluminum in wet hydrogen.

FIGURE 15. *(a) Crystallographic terraces on a {0001} section thinned by heating in dry hydrogen for 90 min at 1450 °C; (b) prism plane dislocations of edge character normal to the surface of a thermally thinned {0001} section.*

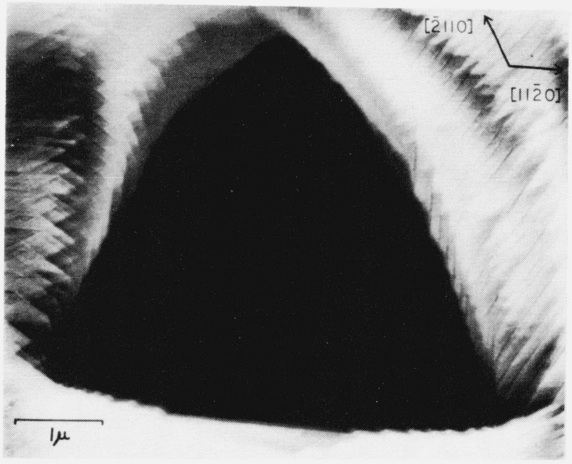

FIGURE 16. *Etch hillock on a basal section thinned by heating in dry hydrogen for 90 min at 1450 °C.*

Diffraction data from the whiskers found in the present work indicates that they were not α-aluminum oxide.

In contrast with the foregoing examples, samples thinned in a stream of dry hydrogen for $1\frac{1}{2}$ hr at 1450 °C were free from visible 'contamination,' and moreover, exhibited surface terraces which were strictly parallel to crystallographic directions. Terraces of $\langle 11\bar{2}0\rangle$ and $\langle 10\bar{1}0\rangle$ type are illustrated in figure 15a. The only dislocations observed in these samples were short segments normal to the $\{0001\}$ planes. These segments did not move during the thinning process, and it must be assumed that they were prism plane dislocations. Examples, some of which are marked by arrows, are seen in figure 15b, near the extinction contours; these dislocations must be edge in character. Compared with similar instances seen in chemically thinned specimens, the dislocations were notable for the marked sharpness of the contrast associated with their strain fields. There were no thermal etch pits associated with the dislocations.

Figure 16 shows a thermal etch pip on another sample thinned in dry hydrogen. The terraces surrounding the hillock show all six possible $\langle 11\bar{2}0\rangle$ and $\langle 10\bar{1}0\rangle$ orientations and the hillock's edges are roughly parallel to $\langle 11\bar{2}0\rangle$ directions. It is believed that these etch pips are centered on spots where surface impurities (for example, small amounts of $AlPO_4$ or $Al(PO_3)_3$ left after chemical thinning) cause the motion of terraces to be impeded and slowed down. Elsewhere the crystal continues to thin. Etch hillocks are not restricted to the surfaces of thermally thinned samples, but can appear after chemical dissolution. Therefore, the hillock shown in figure 16 may have been present in embryo form before evaporation took place, and this treatment served only to enlarge it.

In the course of hot stage work in the microscope, it was possible to observe evaporation *in vacuo* directly. From these experiments, we conclude that the process leads to surface features closely resembling those found after evaporation in hydrogen. Figures 17a and 17b show the same area before and after heating to a temperature of $\sim$1750 °C for a period of about 3 min. In the second figure, many crystallographic terraces are visible and, at the specimen edge, the receding terraces have left frondlike promontories. Traces of the carbon backing film are visible in places; during heating, it shrinks and coarsens. No hillocks were seen on specimens thinned in the microscope. This may be either because the heating period was too short for their formation, or because nucleating particles of contaminant are removed by heating *in vacuo*.

A striking feature of all the thermally thinned samples is the appearance of the associated electron diffraction patterns. The specimens are usually of such a thickness that they produce patterns containing strong Kikuchi lines, which are easily visible against a fairly uniform elastic continuum. Near the primary beam many fine dark deficiency lines are resolved, corresponding to Bragg reflections of very high angle.

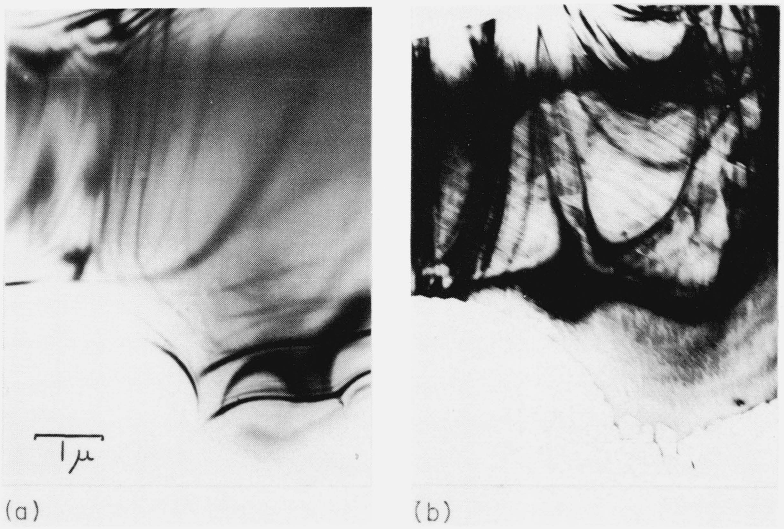

FIGURE 17. *Appearance of a $\{0001\}$ section: (a) before heating in the electron microscope; (b) after heating to $\sim$ 1750 °C for 3 min.*

Such detail is only obtained with the thermally thinned samples. Its significance stems from the fact that the resolution of Kikuchi patterns is normally limited by the lattice strain in regions of the diffracting surface from which the beam emerges. Sample bending as little as 1 part in 10^4 can destroy detail. Our observations suggest two possibilities: (a) chemically thinned samples are covered with a distorting layer of contaminant, which is absent on thermally thinned samples; (b) thermally thinned samples are more strain-free than normal samples. Of these, we favor explanation (b). The excellent contrast around prism plane dislocations in thermally thinned specimens also suggests that the only internal strains are those localized around defects. It is quite reasonable to expect that unannealed chemically thinned sections, produced from a massive boule or rod, will exhibit some internal strain.

4. Conclusions

The nature of etch features on the surfaces of single crystal sapphire have been demonstrated by optical and electron transmission microscopy. Chemical etch pits are found to reveal the symmetry of the etched surface, as anticipated. On the basal plane, pits produced by the action of hot phosphoric acid are three-sided, with the etch-pit edges parallel to $<11\bar{2}0>$ directions. Hexagonal etch pits produced by hot potassium hydroxide are more distinct than the three-sided pits and their edges are parallel to $<10\bar{1}0>$ directions. Within crystal subgrains there is a good correspondence between etch pits and dislocations emerging at the surface. Along subgrain boundaries, the correspondence often breaks down.

Etch tunneling down dislocation lines is sometimes seen in nominally pure sapphire. It is a stiking feature of etched crystals of impurity-doped sapphire, particularly ruby. The tunneling effect is attributed to the presence of impurity atmospheres or even microsegregation at grown-in dislocations.

The chemical dissolution of star sapphire ($Al_2O_3 + TiO_2$) has been studied, and optical observations have been compared with those made in the electron microscope. From these observations it is concluded that the precipitates are surrounded by a zone depleted in solute. On dissolution of the crystal surfaces, the depleted zones lead to the production of etch hillocks surrounding precipitate sites. The hillocks have triangular and lozenge-shaped forms. Triangular hillocks are found to result from dissolution around small precipitates with a triangular profile, while the elongated forms are associated with needles.

The characteristics of crystal surfaces etched in certain gas atmospheres have been studied to see if there is any correlation between internal and surface defects. Under the experimental conditions realized, no correlation is found, although it might be expected for very slow rates of attack. Nitrogen and argon atmospheres (of tank purity) produce 'contaminated' surfaces, exhibiting curving terraces having no relation to the crystallography of the surface. Samples etched in dry hydrogen, or in the vacuum of the electron microscope, show similar features and they are relatively clean. Moreover, they are covered with well defined crystallographic terraces; most of these are parallel to $<11\bar{2}0>$ directions, but there are also many examples parallel to $<10\bar{1}0>$ directions. From comparison of Kikuchi line patterns for chemically and for thermally thinned samples, it is concluded that the heat-treatment effectively removes long-range internal strains. This is further demonstrated by the clarity with which the strain fields are revealed around prism plane dislocations.

Our results confirm that electron transmission microscopy is a powerful method of correlating internal and surface features. Even with a relatively inert material like sapphire, treatments can be devised to etch defect structures selectively and the early stages of attack are easily discerned in the electron microscope.

Our thanks are due to W. S. Brower for supplying boules of impurity-doped sapphire, and to A. C. Bonanno for careful preparation of the micrographs. The work was partially supported by the Advanced Research Projects Agency.

5. Appendix. Extinction Distances in α–Al_2O_3

The dynamical theory of electron diffraction, developed in recent years by Heidenreich [17], Howie and Whelan [18], and others has had many successes in explaining the diffraction contrast seen in transmission specimens. In particular, the theory accounts for the equal thickness fringes seen in wedge-shaped crystals when only one set of lattice planes is diffracting. When the incident beam strikes the crystal at almost a Bragg angle, the transmitted and diffracted beam intensities vary with depth of crystal penetration, z, as

$$I = \frac{\sin^2 \pi z\, (t_g^{-2} + s^2)^{1/2}}{(t_g^{-2} + s^2)}$$

where t_g is called the extinction distance and s is the distance of the reciprocal lattice points, defined by $\mathbf{g}$, from the surface of the Ewald sphere.

The electron image from a wedge-shaped crystal therefore exhibits extinction contours at intervals corresponding to thickness increments of $(t_g^{-2} + s^2)$. The increment is a maximum t_0 when the specimen is exactly oriented at the Bragg angle ($s = 0$).

Unlike some metals, aluminum oxide crystals lack well-characterized defects from which, with the aid of diffraction data, extinction distances could be estimated for various diffracting planes. Moreover, direct comparison of optical and electron interference fringes, used by Frankl [19] for silicon, is less practical for aluminum oxide on account of its refractive index.

Values of t_0 have been calculated, therefore, using an expression of Whelan and Hirsch [20]:

$$t_0 = \frac{\lambda E}{V_g}$$

where E is the accelerating potential of the electron beam, λ is the wavelength and V_g is the Fourier coefficient of lattice potential, expressed in volts, for the diffracting planes. The Fourier coefficient is a measure of elastic scattering from the partially screened nuclear fields at the atomic centers in the lattice; it can be calculated, therefore, by a correct summation of the electron scattering factors for the individual atoms in the unit cell. With appropriate substitutions, the value of V_g is found to be

$$V_g = \frac{600\ \mathrm{h}^2 d_g^2 \sin^2 \theta}{\pi m e V \lambda^2} \Sigma f_j \exp\left(-2\pi i \mathbf{g} \cdot \mathbf{r}_j\right)$$

where h is Planck's constant, m the mass of the electron, e the electronic charge, V the volume of the unit cell, d_g the interplanar spacing associated with the Bragg reflection $\mathbf{g}$ at Bragg angle θ, and f_j the electron scattering factor for the jth atom at $\mathbf{r}_j$ in the unit cell. The summation $\Sigma f_j \exp(-2\pi i \mathbf{g} \cdot \mathbf{r}_j)$ is the structure factor for electrons, F. The latter, and hence V_g, was simply calculated for the rhombohedral cell using the atomic coordinates given by Kronberg [21] and the electron scattering amplitudes, f_j, calculated by Ibers as given by Thomas [22]. The latter were obtained using Hartree-Fock screening models for the aluminum and oxygen atoms.

Extinction distances thus obtained, corrected for the relativistic electron momentum are given in the following table:

Rhombohedral indices	$10\bar{1}$	$2\bar{1}\bar{1}$	111	222
Hexagonal indices	$11\bar{2}0$	$30\bar{3}0$	0003	0006
Extinction distance, t_0 (angstroms)	1260	815	∞	650

These values are probably about 10 percent low, owing to a further relativistic correction which has been omitted. Fowler and Marton [23] have recently pointed out that the accelerating potential for electrons, E, should be replaced by the 'effective relativistic potential difference' E^*, where $E^* = E + \frac{e}{2m_0c^2}E^2$. This correction amounts to $\sim +10$ percent for 100 kV electrons; previously it has been neglected in calculations of extinction distances.

6. References

[1] W. G. Johnston, Progr. Ceramic Sci. **2,** 1 (1961).
[2] J. D. Livingston, Acta Met. **10,** 229 (1962).
[3] D. J. Barber and N. J. Tighe, Phil. Mag. **11,** 495 (1965).
[4] J. B. Wachtman and L. H. Maxwell, J. Am. Ceram. Soc. **37,** 291 (1954); **40,** 377 (1957).
[5] M. V. Klassen-Neklyudova, J. Tech. Phys. (U.S.S.R.) **12,** 519, 535 (1942).
[6] R. Scheuplein and P. Gibbs, J. Am. Ceram. Soc. **43,** 458 (1960); **45,** 439 (1962).
[7] M. Seebach, Neues Jahrb. Mineral Geol. **A54,** 420 (1926).
[8] D. L. Stephens and W. J. Alford, J. Am. Ceram. Soc. **47,** 81 (1964).
[9] H. Palmour, J. J. DuPlessis and W. W. Kriegel, J. Am. Ceram. Soc. **44,** 400 (1961).
[10] N. J. Tighe, Rev. Sci. Inst. **35,** 520 (1964).
[11] A. P. Honess, The Nature, Origin and Interpretation of Etch Figures on Crystals (John Wiley & Sons, New York, N.Y., 1927).
[12] D. J. Barber and E. N. Farabaugh, J. Appl. Phys. (in press).
[13] D. J. Barber, J. Appl. Phys. **35,** 3084 (1964); ibid. (in press).
[14] E. M. Levin, H. F. McMurdie and C. R. Robbins, Phase diagrams for ceramists, p. 121 (American Ceramic Society Inc., Columbus, Ohio, 1964).
[15] E. J. Gubelin, Inclusions as a means of gemstone identification, (Gemological Institute of America, 1953).
[16] S. M. Irving, private communication.
[17] R. D. Heidenreich, J. Appl. Phys. **20,** 993 (1943).
[18] A. Howie and M. J. Whelan, Proc. Roy. Soc. (London) **A263,** 217 (1961).
[19] D. R. Frankl, J. Appl. Phys. **35,** 217 (1964).
[20] M. J. Whelan and P. B. Hirsch, Phil. Mag. **2,** 1303 (1957).
[21] M. L. Kronberg, Acta Met. **5,** 507 (1957).
[22] G. Thomas, Transmission Microscopy of Metals, p. 290 (John Wiley & Sons, Inc., New York, N.Y., 1962).
[23] H. A. Fowler and L. Marton, J. Appl. Phys. (in press).

(Paper 69A3–346)